Supplementary Materials for
Generation of Nonuniform Spatiotemporal Optical Vortices and Angular-Momentum Breathing States

Dawei Liu[1†], Xingyuan Zhang[2†], Daijun Luo[1], Huiming Wang[3],
Zhirong Tao[4], Dana JiaShaner[1], Yonghang Tai[5], Zhensheng Tao[6],
Xiaoshi Zhang[7], Zhigang Peng[8], Guangyu Fan[1*], Qiwen Zhan[1,2,9],
[1]School of Optical-Electrical and Computer Engineering,
University of Shanghai for Science and Technology, 200093, Shanghai, China.
[2]Zhejiang Key Laboratory of 3D Micro/Nano Fabrication and Characterization,
Department of Electronic and Information Engineering, School of Engineering,
Westlake University, Hangzhou, Zhejiang 310030, China.
[3]Institute of Photonics, TU Wien, Gusshausstrasse 27/387, Vienna, Austria.
[4]Karlsruhe Institute of Technology, Karlsruhe, Germany.
[5]Department of Physics and Electronic,
Yunnan Normal University, Kunming, Yunnan 650000, China
[6]State Key Laboratory of Surface Physics and Department of Physics,
Fudan University, Shanghai 200433, China
[7]Yunnan University, Kunming, Yunnan 650500, China.
[8]Beijing Engineering Research Center of Laser Applied Technology,
Beijing University of Technology, Beijing 100124, China
[9]International Institute for Sustainability with Knotted Chiral Meta Matter (WPI-SKCM2),
Hiroshima University, Higashihiroshima, Hiroshima, 739-8526, Japan.
[*]Corresponding author. E-mail: gfan@usst.edu.cn
[†]These authors contributed equally to this work.

This PDF file includes:

Sections S1 to S3
Figures S1 to S3
References

Supplementary Section 1: Digitalized-Coding Generation of Non-uniform Spatiotemporal Optical Vortices

In the main, NSTOVs were generated using a continuous sinusoidal modulation of the azimuthal phase. To further demonstrate the generality and programmability of our approach, we extend this concept to a fully discretized digitalized-coding scheme, in which the azimuthal phase of the vortex is divided into a set of quantized angular segments. In this method, the total topological phase is partitioned into N discrete levels. Fig S1(a) shows an implementation with six uniformly spaced steps across the full 2π phase. The constructed phase pattern (Fig. S1(b)) consists of six angular sectors separated by abrupt phase jumps. Although the phase is discontinuous locally, the mapping satisfies $\Phi(\theta + 2\pi) - \Phi(\theta) = 2\pi$, ensuring that the global topological charge remains unchanged. Thus, digitalized coding preserves the overall vortex topology while enabling highly programmable local azimuthal structuring.

We evaluate the resulting field in both the temporal and spectral domains, as shown in Fig. S1(c). In the temporal domain, the NSTOV exhibits six well-defined intensity lobes along the vortex ring, each aligned with a phase-step boundary. These lobes arise from the locally enhanced azimuthal energy flow induced by the discrete phase gradients. Within each segment, the phase varies smoothly, while finite jumps appear at the interfaces, forming a clearly quantized helical phase profile. In the spectral domain, the amplitude distribution remains similar to that of a conventional spatiotemporal vortex, typically exhibiting a two-lobed structure. Only minor local rearrangements of spectral intensity occur, and the spectral phase retains a discrete angular pattern consistent with its temporal counterpart. This indicates that digitalized coding predominantly redistributes the azimuthal energy flow while leaving the global spectral envelope largely unaffected.

These results confirm that NSTOVs can be generated not only through continuous angular mappings but also through fully digitalized, programmable phase coding. The digitalized-coding strategy substantially broadens the design space of spatiotemporal structured light, offering a robust and versatile platform for reconfigurable topological field engineering [1, 2], multidimensional optical encoding [3, 4], and programmable space–time photonics [5, 6].

Supplementary Section 2: Modal Decomposition and Analytical Description of Spatiotemporal Dynamics

The azimuth-dependent phase profile imposed by the spatial light modulator (SLM) is defined as:

$$\Phi_{\text{SLM}}(k_x, \omega) = \ell[\theta + \alpha \sin(m\theta)], \tag{S1}$$

where $\theta = \arctan[(\omega - \omega_0)\tau_0/(k_x w_0)]$ is the spectral azimuthal angle in the normalized spatiotemporal frequency domain. Here, ω_0 denotes the central angular frequency, while w_0 and τ_0 represent the characteristic spatial beam waist and temporal pulse duration used to nondimensionalize the orthogonal spectral coordinates. The parameter ℓ denotes the topological charge governing the global phase winding. The bracketed terms introduce a deterministically controlled anisotropy: α represents the dimensionless modulation depth, which dictates the amplitude of the local phase distortion, and m is the azimuthal modulation order, which determines the m-fold rotational symmetry of the resulting spatiotemporal lattice.

To elucidate the spectral composition of this structured field, we analyze the corresponding complex spectral transfer function imposed by the SLM, denoted as $M(\theta)$: $M(\theta) = \exp[i\Phi_{\text{SLM}}] = e^{i\ell\theta} \cdot e^{i\ell\alpha \sin(m\theta)}$. By applying the Jacobi-Anger expansion identity, $e^{iz\sin\psi} = \sum_{q=-\infty}^{\infty} J_q(z) e^{iq\psi}$, and identifying the arguments as $z = \ell\alpha$ and $\psi = m\theta$, the anharmonic modulation term can be decomposed into a coherent superposition of infinite integer-order Bessel functions. Consequently, the total spectral field becomes:

$$M(\theta) = e^{i\ell\theta} \sum_{q=-\infty}^{\infty} J_q(\ell\alpha) e^{iqm\theta} = \sum_{q=-\infty}^{\infty} J_q(\beta) e^{i(\ell+qm)\theta}, \tag{S2}$$

where $J_q(\,\cdot\,)$ is the Bessel function of the first kind of order q, and $\beta = \ell\alpha$ serves as the effective modulation index. This expansion reveals that the generated field is spectrally constructed from a central carrier mode (charge ℓ) interfering with a series of discrete sidebands with topological charges $\ell_q = \ell + qm$.

The derivation begins in the frequency domain, where we assume a spectrum corresponding to a pure phase modulation. This electric field distribution, denoted as $\tilde{E}(k, \theta)$, is defined by the product of a Gaussian envelope and an azimuthal phase term: $\tilde{E}(k, \theta) = \exp(-k^2) \cdot e^{i\ell\theta}$, where k represents the normalized radial spectral coordinate, θ is the spectral azimuthal angle, and the integer ℓ indicates the topological charge (vortex order) of the field. To transition to the physical spatiotemporal domain, we apply a 2D Fourier transform, which corresponds to an ℓ-th order Hankel transform for the radial component (mapping the spectral phase $e^{i\ell\theta}$ to the spatial phase $e^{i\ell\phi}$). This yields the radial distribution $R(r)$, expressed as the integral: $R(r) \propto i^{\ell} \int_0^{\infty} k \cdot e^{-k^2} \cdot J_{\ell}(kr)\, dk$. In this expression, r denotes the normalized radial coordinate in the spatiotemporal domain, $J_{\ell}(kr)$ is the Bessel function of the first kind of order ℓ, and i is the imaginary unit. Notably, the factor i^{ℓ} is mathematically significant and corresponds directly to the Gouy phase shift observed in the numerical implementation. By utilizing Weber's second exponential integral and performing identity transformations, we arrive at the exact analytical solution for the radial profile involving Modified Bessel functions (I_{ν}).

Defining a dimensionless variable ξ to scale the solution relative to the characteristic beam waist w_0, specifically $\xi = r^2/(2w_0^2)$ where r represents the physical radial coordinate, we can express the complex electric field $E_{\ell}(r, \phi)$ in the spatiotemporal domain. This is achieved by combining the derived radial amplitude with the spatiotemporal azimuthal phase term $e^{i\ell\phi}$:

$$E_{\ell}(r, \phi) = re^{-\xi} \left[I_{\frac{|\ell|-1}{2}}(\xi) - I_{\frac{|\ell|+1}{2}}(\xi) \right] \cdot e^{i\ell\phi} \tag{S3}$$

This specific analytical form is of particular significance as it corresponds to the solution for Hypergeometric Gaussian (HyGG) modes. While HyGG modes provide the theoretical description for this structured field, their standard formulation relies on confluent hypergeometric functions (${}_1F_1$), which are often computationally intensive and slow to evaluate numerically. The expression derived here, utilizing Modified Bessel functions (I_{ν}), serves as a computationally efficient analytical substitute that circumvents these numerical bottlenecks while maintaining mathematical exactness.

Based on the spectral decomposition analyzed above, the total STOV field is constructed by the coherent superposition of the three dominant HyGG modes (corresponding to the central carrier and the first-order modulation sidebands). The total electric field $E_{\text{total}}(r, \phi)$ in the physical spatiotemporal domain can be expressed as:

$$E_{\text{total}}(r, \phi) = C_0 \cdot i^{\ell_0} \cdot \Psi_{\ell_0}(r, \phi) + C_+ \cdot i^{\ell_+} \cdot \Psi_{\ell_+}(r, \phi) + C_- \cdot i^{\ell_-} \cdot \Psi_{\ell_-}(r, \phi), \tag{S4}$$

where i is the imaginary unit, and the factor i^{ℓ} represents the characteristic Gouy phase shift introduced by the Fourier transform. The term $\Psi_\ell(r, \phi)$ denotes the normalized spatial mode function for a specific topological charge ℓ. Incorporating the analytical solution derived previously, the explicit form for each constituent mode is compactly expressed using the dimensionless radial coordinate $\xi = r^2/(2w_0^2)$:

$$\Psi_\ell(r, \phi) = N_\ell \cdot r \cdot e^{-\xi} \cdot \left[I_{\frac{|\ell|-1}{2}}(\xi) - I_{\frac{|\ell|+1}{2}}(\xi) \right] \cdot e^{i\ell\phi}. \tag{S5}$$

In this expression, $I_\nu(\,\cdot\,)$ is the modified Bessel function of the first kind, and N_ℓ is a normalization constant determined numerically to ensure energy conservation (satisfying $\iint |\Psi_\ell|^2 \, r \, dr \, d\phi = 1$).

The specific parameters and weighting coefficients are strictly determined by the Jacobi-Anger expansion. With the effective modulation index defined as $\beta = \ell_0 \alpha$ (where $\ell_0 \equiv \ell$ denotes the fundamental topological charge), the topological charges for the three interacting modes are identified as ℓ_0 (carrier), $\ell_+ = \ell_0 + m$ (positive sideband), and $\ell_- = \ell_0 - m$ (negative sideband). Correspondingly, the amplitude weights are governed by the Bessel functions of the first kind: $C_0 = J_0(\beta)$ for the carrier, $C_+ = J_1(\beta)$ for the $q = +1$ sideband, and $C_- = J_{-1}(\beta) = -J_1(\beta)$ for the $q = -1$ sideband.

It is important to note that while the spectral decomposition theoretically involves an infinite series, the physical field structure is dominated by the lowest-order terms due to the rapid spectral decay of the coefficients $J_q(\beta)$ at moderate modulation indices. Consequently, the complex field is accurately approximated as the coherent interference of the central carrier (ℓ_0) with the two principal first-order sidebands ($\ell_\pm$).

The superposition of optical vortices with distinct topological charges induces the phenomenon of singularity splitting. Specifically, the coherent interference between the central **carrier mode** of charge ℓ_0 and the sideband modes of charge $\ell_0 \pm m$ generates secondary phase singularities. Within the symmetric three-mode superposition, this interaction produces an azimuthal modulation with m-fold rotational symmetry, resulting in m discrete regions of constructive interference characterized by intensity maxima and m regions of destructive interference manifesting as intensity minima. The radial distribution of these secondary structures is strictly governed by the modulation depth α. Since the sideband-to-carrier amplitude ratios depend on the effective index $\beta = \ell_0 \alpha$, the parameter α functions as a radial control variable. Variation in α causes the secondary vortices to migrate radially relative to the optical axis, thereby altering the spatial mode overlap and modifying the contrast between the peak and valley intensities of the wave packet. Furthermore, this interferometric framework elucidates the formation of steep phase gradients. In regions of low optical intensity corresponding to destructive interference, the modulus of the complex field is minimal. In these zones, the phase evolution becomes highly sensitive to the rapidly varying phase components of the constituent modes, as the stabilizing influence of the field amplitude diminishes. Consequently, the component with the faster phase variation dominates relative to the small local amplitude, inducing abrupt phase transitions. Conversely, high-intensity regions of constructive interference possess a large complex modulus that stabilizes the local phase. Therefore, the steepest phase gradients—and potential additional phase singularities—are physically localized to regions of minimal intensity. To facilitate the quantitative analysis of the azimuthal intensity modulation and the local momentum density, we derive a simplified analytical form of the complex field at a fixed radial distance $r = R$ (typically chosen at the radius of maximum intensity). By fixing the radial coordinate, the radial dependence terms—comprising the Gaussian envelope and the modified Bessel functions—reduce to constant scalar amplitude coefficients.

We define the dimensionless radial coordinate at this specific radius as $\xi = R^2/(2w_0^2)$. By grouping the radial amplitude functions and the Jacobi-Anger expansion coefficients, we introduce three real-valued amplitude parameters, $\mathcal{A}$, $\mathcal{B}$, and $\mathcal{C}$, which characterize the magnitude of the carrier and sideband contributions:

$$\begin{cases} \mathcal{A} = J_0(\beta) N_{\ell_0} \mathcal{R}_{\ell_0}(\xi) \\ \mathcal{B} = J_1(\beta) \left[N_{\ell_+} \mathcal{R}_{\ell_+}(\xi) - N_{\ell_-} \mathcal{R}_{\ell_-}(\xi) \right] \\ \mathcal{C} = J_1(\beta) \left[N_{\ell_+} \mathcal{R}_{\ell_+}(\xi) + N_{\ell_-} \mathcal{R}_{\ell_-}(\xi) \right] \end{cases} \tag{S6}$$

where $\mathcal{R}_\ell(\xi) = Re^{-\xi}[I_{(|\ell|-1)/2}(\xi) - I_{(|\ell|+1)/2}(\xi)]$ represents the unnormalized radial profile for a mode of charge ℓ evaluated at the fixed radius. Here, $\mathcal{A}$ corresponds to the amplitude of the central carrier, while $\mathcal{B}$ and $\mathcal{C}$ represent the weighted difference and sum of the sideband amplitudes, respectively.

Crucially, the coherent superposition involves phase shifts $i^{\ell_\pm}$ relative to the carrier i^{ℓ_0}. Utilizing the relation $\ell_\pm = \ell_0 \pm m$, the relative phase factors can be expressed as $i^{\pm m} e^{\pm im\phi}$. To simplify the trigonometric manipulation, we introduce a rotated azimuthal variable $\tilde{\phi} = m\phi + m\pi/2$. This allows us to absorb the imaginary units into the angular argument, transforming the complex exponential terms into purely real trigonometric functions within the local frame. Consequently, by factoring out the global phase term $i^{\ell_0}e^{i\ell_0\phi}$, the total complex amplitude $E(R,\phi)$ reduces to a compact form with explicitly separated real and imaginary components:

$$E(R,\phi) = i^{\ell_0}e^{i\ell_0\phi} \cdot \left[(\mathcal{A} + \mathcal{B}\cos\tilde{\phi}) + i(\mathcal{C}\sin\tilde{\phi})\right]. \tag{S7}$$

Here, we identify the real and imaginary projection envelopes as $X(\phi) = \mathcal{A} + \mathcal{B}\cos\tilde{\phi}$ and $Y(\phi) = \mathcal{C}\sin\tilde{\phi}$, respectively. This simplified structure reveals that the complex field vector at a fixed radius traces an elliptical trajectory in the complex plane, superimposed on the global rotation of the carrier vortex. The real component $X(\phi)$ describes the amplitude modulation driven by the sideband asymmetry ($\mathcal{B}$), while the imaginary component $Y(\phi)$ is governed by their constructive interference ($\mathcal{C}$). This separation is pivotal for the subsequent derivation of the optical intensity and phase gradient.

Building upon the simplified field projections $X(\phi)$ and $Y(\phi)$, we first determine the azimuthal intensity profile $I(\phi)$, which is rigorously defined by the squared modulus of the complex amplitude:

$$I(\phi) = |E(R,\phi)|^2 = (\mathcal{A} + \mathcal{B}\cos\tilde{\phi})^2 + (\mathcal{C}\sin\tilde{\phi})^2. \tag{S8}$$

This expression mathematically quantifies the m-fold rotational symmetry of the intensity lobes observed in the lattice structure.

Simultaneously, the azimuthal component of the local phase gradient, which characterizes the wavefront curvature and local orbital angular momentum (OAM) flux, is derived from the total phase argument $\Phi = \ell_0\phi + \arctan[Y(\phi)/X(\phi)]$. Applying the chain rule for derivatives, $\partial_\phi \arctan(Y/X) = (X\partial_\phi Y - Y\partial_\phi X)/(X^2+Y^2)$, and noting that $\partial_\phi\tilde{\phi} = m$, we obtain the physical gradient at radius R:

$$\nabla_\phi\Phi = \frac{1}{R}\frac{\partial\Phi}{\partial\phi} = \frac{1}{R}\left[\ell_0 + \frac{m\mathcal{C}(\mathcal{A}\cos\tilde{\phi} + \mathcal{B})}{I(\phi)}\right]. \tag{S9}$$

In the paraxial approximation, the local canonical momentum density $\mathbf{p}$ is proportional to the product of the optical intensity and the phase gradient. Focusing on the azimuthal dynamics, the magnitude $|\mathbf{p}(\phi)| \propto I(\phi)\cdot|\nabla_\phi\Phi|$. Substituting Eq. (S8) and Eq. (S9) into this relationship leads to the exact cancellation of the $I(\phi)$ denominator in the interference term. The final analytical expression for the azimuthal momentum density is:

$$|\mathbf{p}(\phi)| \propto \frac{1}{R}\left|\ell_0 \cdot I(\phi) + m \cdot \mathcal{C} \cdot (\mathcal{A}\cos\tilde{\phi} + \mathcal{B})\right|. \tag{S10}$$

Equation (S10) provides a rigorous decomposition of the momentum transport into two distinct mechanisms. The first term, scaled by the carrier charge ℓ_0, originates directly from the optical intensity distribution $I(\phi)$ and represents the background momentum transport. In contrast, the second term, proportional to the modulation order m, constitutes a gradient-driven flux arising from the steep phase gradients induced by the sideband interference. This decomposition is critical for interpreting the competition between intensity-dominated and phase-gradient-dominated transport regimes.

The analytical structure of Eq. (S10) elucidates the competitive dynamics between the background momentum transport (proportional to $\ell_0 I$) and the gradient-driven flux (proportional to m). Under the specific numerical parameters adopted in this study ($\alpha = 0.5, \ell_0 = 1$), this interplay manifests as two distinct transport regimes. For modulation orders $m \leq 2$, the interference-induced perturbation remains subordinate to the background topological current; consequently, the local energy flow is largely dictated by the photon density, yielding an in-phase correlation where momentum maxima spatially align with intensity maxima. Conversely, for $m \geq 3$, the gradient term becomes dominant. In regions of destructive interference, the depletion of optical intensity is effectively superseded by the steep phase gradients associated with the split singularities. This results in an out-of-phase distribution where the momentum density peaks within local intensity minima. This framework rigorously clarifies the transition from intensity-following to topology-driven transport as a direct consequence of enhanced phase gradients prevailing over local intensity depletion.

Supplementary Section 3: Topological Dynamics of NSTOVs in Frequency-Conversion Processes

NSTOVs offer a directly observable platform for examining the transport, redistribution and global conservation of topological quantities in light, thereby enabling a systematic exploration of the coupling between topological structure and dynamical evolution in continuous space. A central question that follows from this framework is whether the intrinsic local phase-gradient modulation of NSTOVs can be preserved during nonlinear frequency conversion and faithfully transferred to higher-frequency channels. To address this question, we investigate the topological dynamics of NSTOVs in second-harmonic generation (SHG) as a representative model [7–9].

Fig S2 presents the evolution of the angular-momentum distribution for several representative NSTOVs undergoing SHG, under both ideal phase-matching conditions and scenarios including phase-mismatch effects. For an NSTOV with manipulation frequency $m = 1$ and modulation amplitude $a = 0.6$, the fundamental field exhibits a single localized bright sector arising from an enhanced local phase gradient. Notably, this localized feature remains clearly preserved in the SHG output, independent of whether the model assumes perfect phase matching. The persistence of this bright sector indicates that the azimuthal regions of accelerated and decelerated energy flow in the fundamental field, arising from locally increased and decreased phase gradients, are reproduced with high fidelity in the second-harmonic field.

As the manipulation frequency m increases, the number of localized bright sectors in the fundamental NSTOV increases accordingly, exhibiting a well-defined azimuthal periodicity. The SHG results show that this periodic angular structure is fully retained after frequency doubling: the number, position and relative angular spacing of the bright sectors in the second-harmonic field remain identical to those of the fundamental. This behaviour confirms that the local phase-gradient modulation intrinsic to NSTOVs is not washed out during the SHG process but instead transferred to the higher-frequency channel with high fidelity. Taken together, these results demonstrate that the non-uniform azimuthal phase structure of NSTOVs, along with the resulting redistribution of local energy flow, remains remarkably robust in nonlinear frequency conversion. The faithful preservation of local topological features across frequency channels reveals a deep connection among topological phase mapping, energy-flow dynamics and nonlinear up-conversion, and further suggests promising opportunities for engineering controllable topological states and developing multidimensional encoding schemes in multi-wavelength and high-harmonic systems.

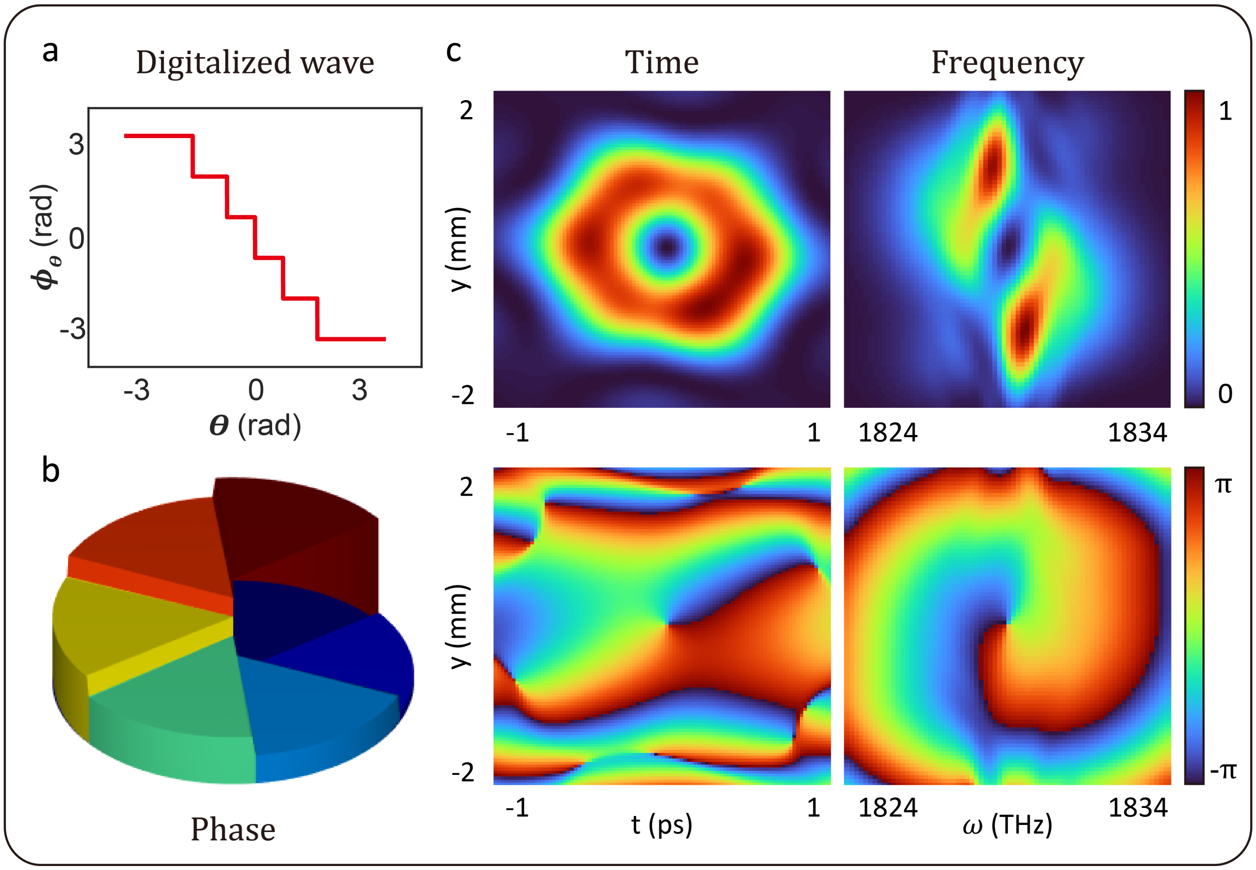

Figure S1: **NSTOVs generated by digitalized phase discretization.** (a) Discrete phase waveform constructed by dividing the full 2π range into six digital step levels. (b) Corresponding azimuthal phase map, showing six angular sectors created by the discretized phase. (c) Temporal and spectral intensity and phase distributions of the NSTOV generated via digital phase discretization, demonstrating faithful mapping of the discrete azimuthal structure into both domains.

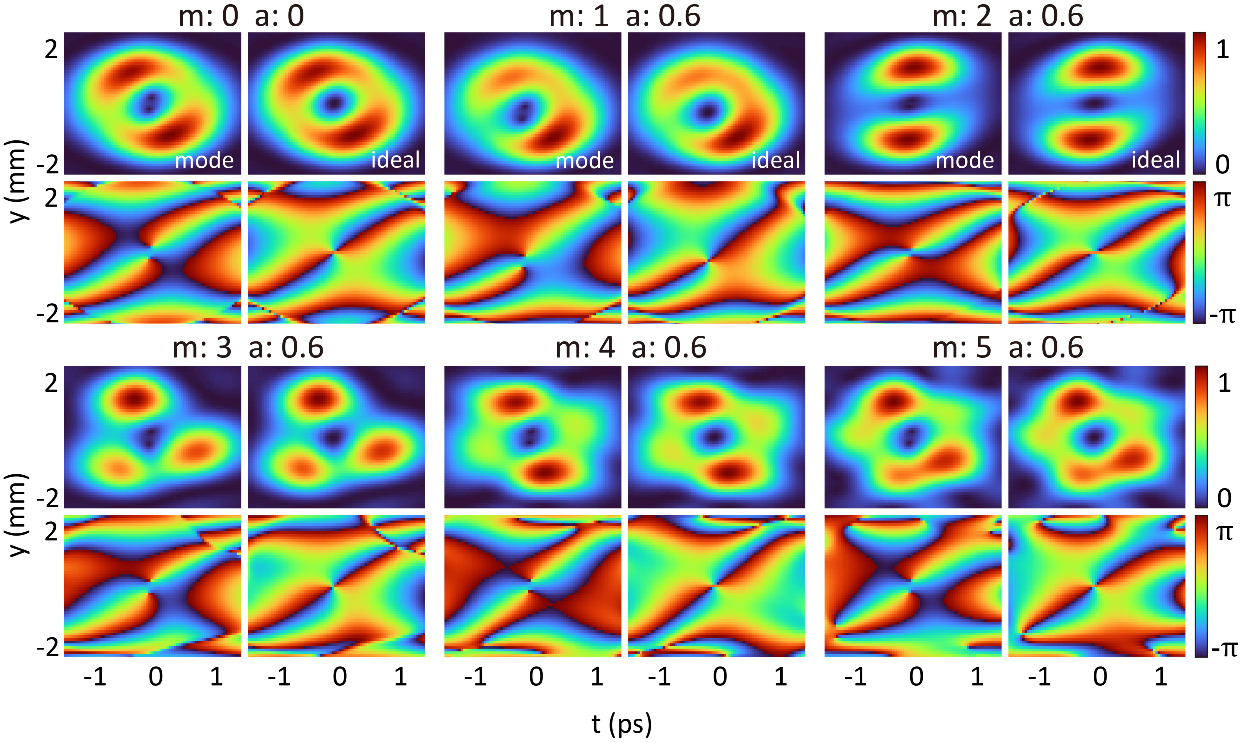

Figure S2: **Dynamics of NSTOVs in SHG processes.** Second-harmonic generation (SHG) results for several types of NSTOVs under both ideal phase-matching conditions and phase-mismatched models, illustrating the preservation and evolution of their characteristic azimuthal features during frequency conversion.

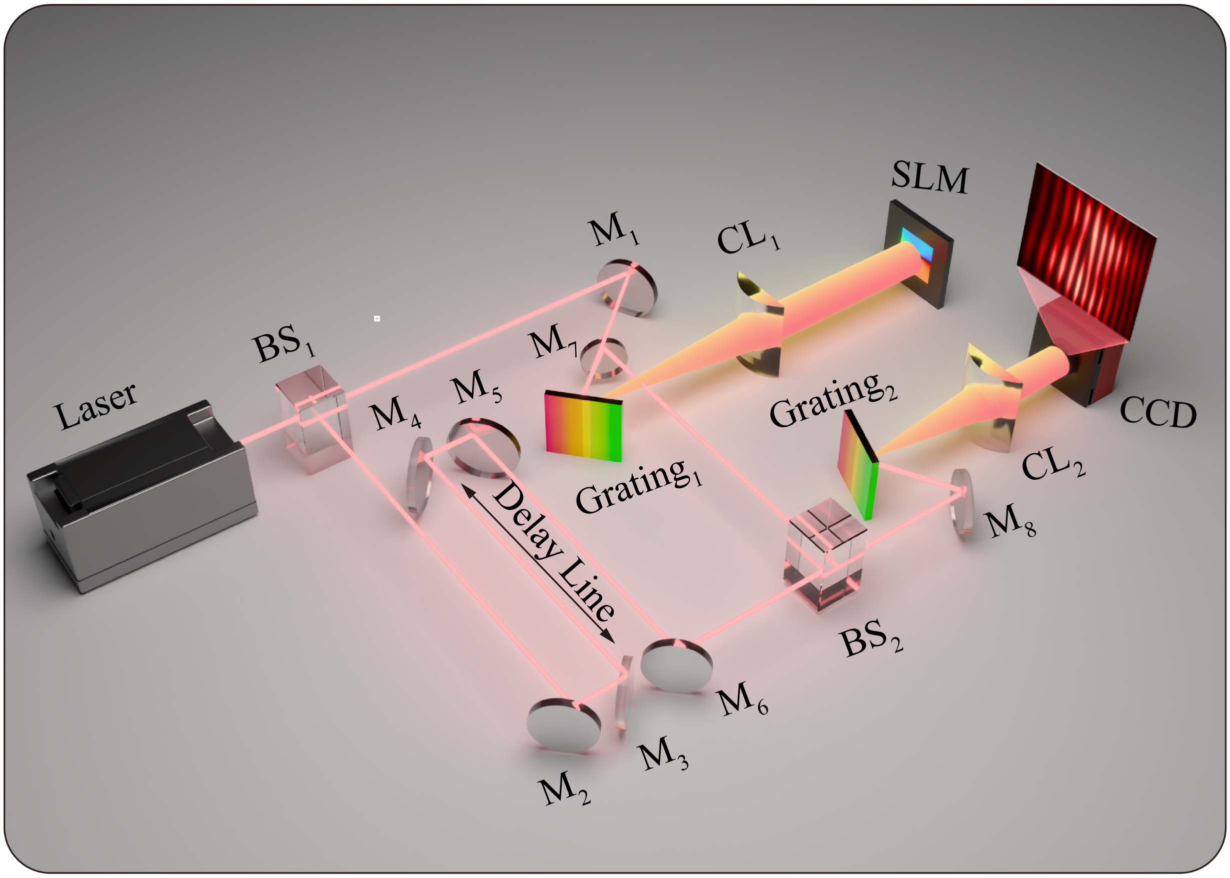

Figure S3: **Experimental setup for the generation and detection of NSTOVs** BS, beam splitter; M, mirror; CL1–2, cylindrical lenses; SLM, spatial light modulator loaded with a non-uniform vortex phase pattern.

References

[1] Daria Smirnova, Daniel Leykam, Yidong Chong, and Yuri Kivshar. Nonlinear topological photonics. *Applied Physics Reviews*, 7(2), 2020.

[2] Chao He, Yijie Shen, and Andrew Forbes. Towards higher-dimensional structured light. *Light: Science & Applications*, 11(1):205, 2022.

[3] Jian Wang, Jeng-Yuan Yang, Irfan M Fazal, Nisar Ahmed, Yan Yan, Hao Huang, Yongxiong Ren, Yang Yue, Samuel Dolinar, Moshe Tur, et al. Terabit free-space data transmission employing orbital angular momentum multiplexing. *Nature photonics*, 6(7):488–496, 2012.

[4] Fengliang Dong and Weiguo Chu. Multichannel-independent information encoding with optical metasurfaces. *Advanced Materials*, 31(45):1804921, 2019.

[5] Christopher L Panuski, Ian Christen, Momchil Minkov, Cole J Brabec, Sivan Trajtenberg-Mills, Alexander D Griffiths, Jonathan JD McKendry, Gerald L Leake, Daniel J Coleman, Cung Tran, et al. A full degree-of-freedom spatiotemporal light modulator. *Nature Photonics*, 16(12):834–842, 2022.

[6] Xianji Piao, Sunkyu Yu, and Namkyoo Park. Programmable photonic time circuits for highly scalable universal unitaries. *Physical Review Letters*, 132(10):103801, 2024.

[7] Yiqi Fang, Shengyue Lu, and Yunquan Liu. Controlling photon transverse orbital angular momentum in high harmonic generation. *Physical Review Letters*, 127(27):273901, 2021.

[8] Guan Gui, Nathan J. Brooks, Henry C. Kapteyn, Margaret M. Murnane, and Chen-Ting Liao. Second-harmonic generation and the conservation of spatiotemporal orbital angular momentum of light. *Nature Photonics*, 15(8):608–613, 2021.

[9] Xuechen Gao, Wenbin Chen, Yuchong Guo, Jintao Fan, Wei Chen, Yanqing Lu, and Minglie Hu. Space–time singularity dynamics for second harmonic spatiotemporal optical vortices. *Advanced Photonics Nexus*, 4(3):036003, 2025.